Fluorescence thermometry enhanced by the quantum coherence of single spins in diamond

David M. Toyli[a], Charles F. de las Casas[a,1], David J. Christle[a,1], Viatcheslav V. Dobrovitski[b], and David D. Awschalom[a,c,2]

[a]Center for Spintronics and Quantum Computation, University of California, Santa Barbara, CA 93106; [b]Ames Laboratory, US Department of Energy, Ames, IA 50011; and [c]Institute for Molecular Engineering, University of Chicago, Chicago, IL 60637

Contributed by David D. Awschalom, April 11, 2013 (sent for review March 26, 2013)

We demonstrate fluorescence thermometry techniques with sensitivities approaching 10 mK·Hz$^{-1/2}$ based on the spin-dependent photoluminescence of nitrogen vacancy (NV) centers in diamond. These techniques use dynamical decoupling protocols to convert thermally induced shifts in the NV center's spin resonance frequencies into large changes in its fluorescence. By mitigating interactions with nearby nuclear spins and facilitating selective thermal measurements, these protocols enhance the spin coherence times accessible for thermometry by 45-fold, corresponding to a 7-fold improvement in the NV center's temperature sensitivity. Moreover, we demonstrate these techniques can be applied over a broad temperature range and in both finite and near-zero magnetic field environments. This versatility suggests that the quantum coherence of single spins could be practically leveraged for sensitive thermometry in a wide variety of biological and microscale systems.

spintronics | electron spin resonance | quantum control

Thermometry based on thermally driven changes in fluorescence lifetimes or intensities is an essential technique in many environments that preclude electrical probes (1). Although typical fluorescence thermometers use millimeter-scale optical probes (2), the desire to noninvasively monitor intracellular thermal gradients has motivated efforts to develop analogous methods at the nanoscale (3, 4). This interest has stimulated the development of nanoscale fluorescence thermometers based on quantum dots (5), rare-earth ions (6), and nanogels (7), with recent studies suggesting that intracellular temperature gradients are on the order of 1 K (8). However, the application of conventional fluorescence thermometry techniques in biological settings is limited by temperature resolutions of ∼0.2 K or worse (8–10), motivating the development of more advanced nanoscale thermometers.

In recent years, solid-state electronic spins have gained considerable attention for applications in nanoscale sensing. In particular, the diamond nitrogen vacancy (NV) center (Fig. 1*A*) has garnered attention for its optical spin initialization and fluorescence-based spin readout (11), the ability to isolate and measure single defects (12), and the ability to manipulate its spin using microwave electron spin resonance techniques (13). NV center sensing is based on monitoring shifts in the spin resonance frequencies through the defect's fluorescence as a function of external perturbations such as magnetic fields (14–17), electric fields (18), or temperature (19, 20), with the sensitivity of these techniques scaling as $1/\sqrt{T_C}$, where T_C is the relevant spin coherence time (21). These coherence times can be enhanced by two to three orders of magnitude for perturbations amenable to time-periodic (AC) modulation through the use of dynamical decoupling techniques that periodically invert the spin state and the signal being sensed to mitigate the effects of low-frequency magnetic noise (22–24). These methods have enabled the detection of single electronic spins (15) and nanoscale nuclear spin ensembles external to the diamond (16, 17), with motivations to extend these techniques to biological systems using NV centers in nanodiamonds (25).

Here we demonstrate that the quantum coherence of a single NV center can enhance thermometry. Our technique relies on the use of dynamical decoupling protocols that manipulate the NV center's spin-one ground state to selectively measure thermally driven shifts in the spin resonance frequencies while suppressing the effects of low-frequency magnetic noise. This allows us to exploit the NV center's long spin coherence for thermometry. We achieve spin coherence times for thermal sensing exceeding 80 μs, resulting in inferred thermal sensitivities of 25 mK·Hz$^{-1/2}$. By combining these prolonged coherence times with improved fluorescence detection (26), we estimate that thermal sensitivities better than 10 mK·Hz$^{-1/2}$ should be achievable. These sensitivities demonstrate the NV center's potential to markedly improve on the ∼0.2-K temperature resolution offered by competing nanoscale fluorescence thermometry techniques (3, 4, 8–10). We execute these measurements in two regimes: in moderate magnetic fields where both spin transitions can be resonantly addressed with separate microwave signals and near zero magnetic field where they can be addressed with a single microwave frequency. Finally, we demonstrate the wide range of operating temperatures for NV center thermometers by performing these measurements at 500 K. Together, these results provide a robust set of protocols for NV center-based thermometry.

Principles of Spin-Based Fluorescence Thermometry

Our work focuses on the precise measurement of the NV center's temperature-dependent crystal field splitting (D) between its $m_S = 0$ and $m_S = \pm 1$ sublevels, as seen in the ground-state spin Hamiltonian (27):

$$H_{NV} = DS_z^2 + g\mu_B \vec{B}\vec{S} + \vec{S}\overline{A}\vec{I}. \quad [1]$$

Here $\vec{S}$ is the electronic spin operator, $g = 2.00$ is the electron g factor, μ_B is the Bohr magneton, $\vec{B}$ is the applied magnetic field, $\overline{A}$ is the hyperfine tensor, and $\vec{I}$ is the nitrogen nuclear spin operator ($I = 1$). Additional considerations regarding Eq. **1**, such as the influence of strain and electric fields, are discussed in *SI Appendix*. The crystal field splitting, ∼2.870 GHz at room temperature, exhibits shifts of −74 kHz/K due to thermal expansion (20) and vibronic interactions (28). Because the D term is second order in S_z, ground-state-level shifts due to changes in temperature can be distinguished from Zeeman shifts (Fig. 1*B*). This point has recently been used to perform NV center magnetometry that is insensitive to temperature drift (29). Here we take the opposite approach to perform thermometry that is robust against the NV center's interactions with its magnetic environment. Our approach is to resonantly manipulate the spin such that at

Author contributions: D.M.T., C.F.d.l.C., D.J.C., V.V.D., and D.D.A. performed research, analyzed data, and wrote the paper.

The authors declare no conflict of interest.

Freely available online through the PNAS open access option.

[1]Present address: Institute for Molecular Engineering, University of Chicago, Chicago, IL 60637.

[2]To whom correspondence should be addressed. E-mail: awsch@uchicago.edu.

This article contains supporting information online at www.pnas.org/lookup/suppl/doi:10.1073/pnas.1306825110/-/DCSupplemental.

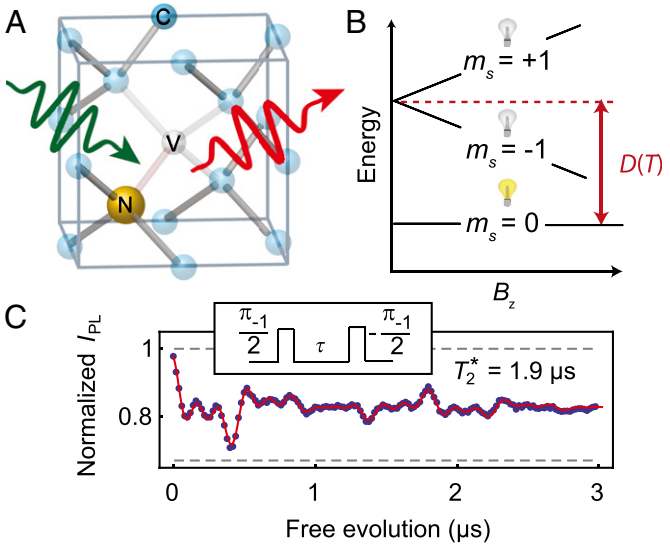

Fig. 1. Nitrogen vacancy center in diamond. (*A*) Depiction of a nitrogen vacancy (NV) center in the diamond lattice. The wavy green arrow represents the 532-nm laser used for optical excitation and the wavy red arrow represents the phonon-broadened fluorescence used to measure the spin state. (*B*) Fine structure of the NV center ground state as a function of axial magnetic field. The light bulbs represent the relative fluorescence difference for the $m_S = 0$ and $m_S = \pm 1$ states. Temperature changes shift the crystal field splitting (D), whereas magnetic fields (B_z) split the $m_S = \pm 1$ sublevels. This difference enables dynamical decoupling pulse sequences that move the spin between all three states to selectively measure temperature shifts and mitigate magnetic noise. (*C*) Ramsey measurement performed on the $m_S = 0$ to $m_S = -1$ transition ($B_z = 40$ G). *Inset* illustrates the pulse sequence. The short inhomogeneous spin lifetime (T_2^*) limits the sensitivity of conventional NV center thermometry. The uncertainties in I_{PL}, estimated from the photon shot noise, are ~0.003. The microwave carrier frequency was detuned from the $m_I = 0$ hyperfine resonance by ~3.5 MHz to induce oscillations in I_{PL}. The fluorescence signal exhibits a beating caused by the three hyperfine resonances and weak coupling to a nearby ^{13}C spin. Gray dashed lines show the fluorescence intensity of $m_S = 0$ and $m_S = -1$ as determined by independent measurements.

specific times the relative phase of the spin states in the laboratory frame becomes e^{-iDt}, where t is the spin's total free evolution time. As this phase is independent of the magnetic field (up to fluctuations on the timescale of the interpulse delay, τ), it is protected from the low-frequency magnetic fluctuations that limit the coherence to the inhomogeneous spin lifetime (T_2^*). Similarly, the phase is independent of the nitrogen nuclear spin state, thus eliminating interference effects observed with conventional Ramsey measurement techniques used to sense static (DC) shifts in the resonance frequencies (Fig. 1*C*). This relative phase is then converted into a population difference of the spin sublevels and measured through the fluorescence intensity (I_{PL}). The fluorescence is ~30% greater for the $m_S = 0$ state than for the $m_S = \pm 1$ states, and varies linearly with the $m_S = 0$ spin population, providing a direct measurement of the NV center spin. This measurement sequence is repeated until the desired level of I_{PL} is reached. As a function of t, the I_{PL} signal oscillates between $I_{PL}(m_S = 0)$ and $I_{PL}(m_S = \pm 1)$ with a frequency given by $D - \Omega_{REF}$, where Ω_{REF} corresponds to the microwave carrier frequencies used for spin manipulation. Small thermally driven changes in D (as well as the value of D itself) can therefore be measured through large changes in the NV center's fluorescence.

Fluorescence Thermometry in Finite Magnetic Fields

We first demonstrate "thermal" analogs to conventional Hahn echo and Carr–Purcell–Meiboom–Gill (CPMG-N) pulse sequences (30) in finite magnetic fields, where both the $m_S = 0$ to $m_S = -1$ and $m_S = 0$ to $m_S = +1$ transitions are resonantly addressed. After optically initializing the spin into the $m_S = 0$ sublevel with a 2-μs laser pulse, we apply one of the pulse sequences shown in Fig. 2*A*, referred to here as the thermal echo (TE) and thermal CPMG-N (TCPMG-N). These pulse sequences follow the same general methodology: The spin is first initialized into a superposition of two of its three eigenstates and then undergoes periods of free evolution punctuated by operations of the form $\pi_{+1}\pi_{-1}\pi_{+1}$ or $\pi_{-1}\pi_{+1}\pi_{-1}$, where the subscripts indicate the spin transition being addressed; e.g., π_{-1} acts on the $m_S = 0$ to $m_S = -1$ transition. These operations interchange the spin populations in the $m_S = +1$ and $m_S = -1$ states, thus inverting the NV center spin state. As a result of the inversions, the $m_S = +1$ and $m_S = -1$ states acquire a total phase e^{-iDt}, which is independent of static magnetic fields and low-frequency magnetic noise. The final microwave pulse converts this phase into

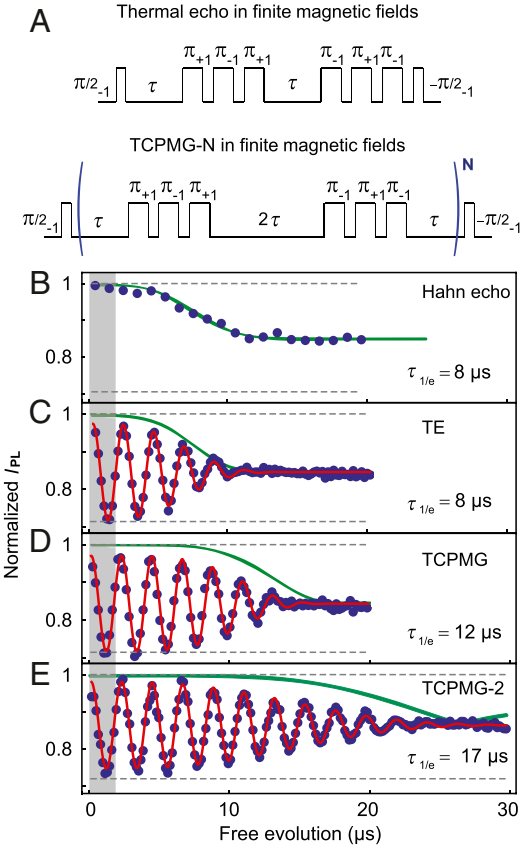

Fig. 2. Thermal echo (TE) and thermal CPMG-N (TCPMG-N) pulse sequences in finite magnetic fields. (*A*) Diagram showing the pulse sequences. Here a π pulse has a duration such that it will invert the spin population between the two sublevels that are resonantly addressed. The subscripts indicate the spin transition being addressed. (*B*) Hahn echo measurement ($m_S = 0$ to $m_S = -1$ transition) at $B_z = 30$ G showing I_{PL} as a function of the free evolution time (2τ for the Hahn echo and TE, 4τ for TCPMG, and 8τ for TCPMG-2). The measurement demonstrates the coherence collapse caused by the incoherent precession of the ^{13}C spin bath. The width of the shaded gray region represents T_2^*. *C*, *D*, and *E* show TE, TCPMG, and TCPMG-2 measurements, respectively, performed at 297.00 K (*SI Appendix*). The uncertainties in I_{PL}, estimated from the photon shot noise, are ~0.005. To induce oscillations in I_{PL} to clearly observe the signal envelope, the average microwave carrier frequency (Ω_{REF}) was detuned from D by ~0.5 MHz. The solid red lines are best fits to the data and the 1/e decay times ($\tau_{1/e}$) are noted on the plots. The observed coherences are in good agreement with numerical modeling (solid green lines). For the TCPMG-2 sequence the coherence time is ninefold greater than T_2^*. For these experimental conditions we infer the thermal sensitivity (η) is 54 ± 1 mK·Hz$^{-1/2}$. Enhancements in the photon collection efficiency could improve η to ~15 mK·Hz$^{-1/2}$ (*Methods*).

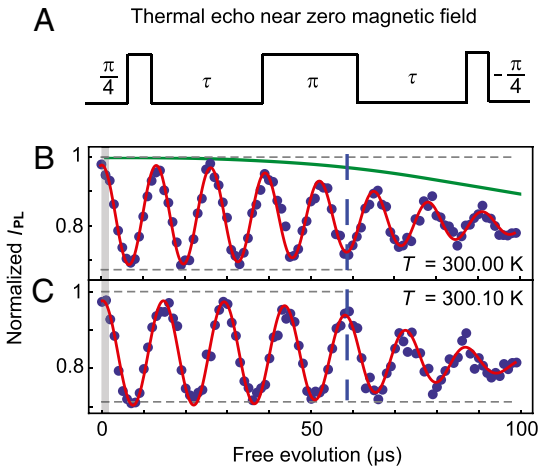

Fig. 3. Thermal echo sequence near zero magnetic field. (*A*) Diagram showing the thermal echo pulse sequence near zero magnetic field when the frequency separation of the $m_S = \pm 1$ sublevels is less than the bandwidth of the microwave pulse used to address the transitions (25 MHz). Here a π pulse has a duration such that the spin, initialized into $m_S = 0$, goes through a superposition of the $m_S = \pm 1$ states and returns to $m_S = 0$ with an opposite sign. (*B*) Thermal echo measurement at 300.00 K. The microwave carrier frequency (Ω_{REF}, 2.87016 GHz) was detuned from *D* by ~75 kHz to induce oscillations in the signal to observe the coherence envelope. The solid green line shows the coherence predicted by the numerical modeling. The width of the shaded gray region represents T_2*. (*C*) The same measurement as in *B*, but with the sample temperature at 300.10 K. The shift in *D* results in a pronounced difference in the signal frequency, leading to large I_{PL} differences at long times (dashed blue line). For both measurements $\tau_{1/e}$ is ~85 μs, and the uncertainties in I_{PL}, estimated from the photon shot noise, are ~0.02. For reference, for these data the measurement time per point was 50 s. From the observed coherence times we infer $\eta = 25 \pm 2$ mK·Hz$^{-1/2}$ for these experimental conditions; we estimate that enhanced photon collection efficiencies could improve η to ~7 mK·Hz$^{-1/2}$. The frequency difference for the oscillations in *B* and *C*, inferred from the fits, is 8 ± 2 kHz, in good agreement the expected value, ~7.4 kHz (20).

a population of the $m_S = 0$ state, which is measured optically. The key difference between the TE and the TCPMG-N sequences is that the TCPMG-N sequences invert the spin more frequently (2N times) and thus counteract higher-frequency magnetic noise. Note that the final $\pi_{-1}\pi_{+1}\pi_{-1}$ operation in the TE sequence compensates for undesired phases acquired during the duration of the π pulses and the interpulse delays (see *SI Appendix* for further details). The TCPMG-N sequences also include two symmetrized $\pi_{-1}\pi_{+1}\pi_{-1}$ operations per period, compensating for these undesired phase accumulations and providing better protection from noise (31).

We apply these pulse sequences to a single NV center in a diamond with natural ^{13}C abundance (1.1%) in a magnetic field ($B_z = 30$ G). In these materials the ^{13}C nuclear spins ($I = 1/2$) are the primary source of decoherence, limiting T_2* to a few microseconds. Conventional Hahn echo measurements can extend the coherence to hundreds of microseconds, but are limited by the incoherent precession of the ^{13}C nuclei, which causes the coherence to collapse and revive at the ^{13}C Larmor frequency (32). Previous studies demonstrated that dynamical decoupling sequences, such as CPMG-N, can counteract the ^{13}C precession to maintain coherence over significantly enhanced timescales (23), and here we demonstrate that this coherence can be accessed for DC thermal sensing. Our focus is on extending the timescale of the first coherence collapse, because our three-level pulse protocols lead to three incommensurate ^{13}C precession frequencies that do not produce the coherence revivals observed in the two-level Hahn echo (33). Fig. 2*B* shows the Hahn echo coherence, with the width of the gray shaded region corresponding to the spin's T_2*. The TE sequence achieves a coherence time similar to that of the Hahn echo sequence, approximately four times greater than T_2* (Fig. 2*C*). The TCPMG (Fig. 2*D*) and TCPMG-2 (Fig. 2*E*) sequences extend the spin coherence even further in time. The coherence time reaches 17.6 μs for TCPMG-2, corresponding to a ninefold improvement in coherence over T_2* and a threefold improvement in thermal sensitivity (η) compared with a Ramsey measurement. Using Eq. **4** described in *Methods*, which is based on monitoring thermally driven changes in I_{PL} at the free evolution time that mutually optimizes the coherence and accumulated phase, we infer that for these experimental parameters $\eta = 54 \pm 1$ mK·Hz$^{-1/2}$. Combining our observed coherence with higher photon collection efficiencies achieved in scanning diamond magnetometers (34) could improve η to ~15 mK·Hz$^{-1/2}$.

Our measurements show good agreement with the results of numerical modeling for the spin dynamics of an NV center in a ^{13}C spin bath subjected to the TE and TCPMG-N sequences (solid green lines in Fig. 2 *B*–*E*; see *Methods* for further details). We note that the difference between the modeling results and the experimental data is larger for the sequences involving more pulses, suggesting that they are caused by pulse imperfections. Interestingly, the simulations for TCPMG-2 (Fig. 2*E*) show a distinct feature near 25 μs, when the coherence collapses and then revives with a 180° shift in phase in the oscillations. We have observed similar behavior on other NV centers in our diamond sample (*SI Appendix*) and tentatively attribute these features to coupling to the most proximal ^{13}C nuclei (32). The overall correspondence between the coherence observed in the measurements and that observed in the numerical simulations supports the assertion that the ^{13}C nuclear spins are a primary limiting factor for these measurements. These observations suggest that the ^{13}C dynamics could be further suppressed to produce improved thermal sensitivities not only through the application of higher-order TCPMG-N sequences, but also by reducing the magnetic field to lower the ^{13}C precession frequency.

Fluorescence Thermometry Near Zero Magnetic Field

Near zero magnetic field, the bandwidth of the resonant microwave pulses exceeds the spectral width of the $m_S = +1$ and $m_S = -1$ resonances, and the thermal echo can be performed with a single microwave source (Fig. 3*A*). We consider near zero magnetic fields ($B_z \sim 0.5$ G) to mitigate mixing of the $m_S = \pm 1$ states induced by transverse strain (18). In this limit the TE sequence has an analogous form to that of pulse sequences proposed for NV center timekeeping (35), where the π pulse that inverts the spin state has a duration such that a spin initially in $m_S = 0$ goes through a superposition of $m_S = \pm 1$ and returns to $m_S = 0$ with an opposite sign.

In this small magnetic field, the TE sequence produces a longer coherence time of ~85 μs (Fig. 3*B*), in good agreement with numerical simulations. This improves the inferred η to 25 ± 2 mK·Hz$^{-1/2}$ for these measurements and we estimate that improved fluorescence detection techniques could improve η to ~7 mK·Hz$^{-1/2}$. To show the sensitivity of this coherence to temperature shifts, we perform a direct experimental demonstration where we increase the temperature of the diamond substrate by 0.1 K while keeping the microwave carrier frequency (Ω_{REF}) fixed (Fig. 3*C*). The change in the accumulated phase of the $m_S = +1$ and $m_S = -1$ states produces a pronounced change in the I_{PL} signal—the dashed blue line spanning Fig. 3 *B* and *C* draws attention to when the two signals have opposite phase. As the 0.1-K shift is clearly resolved, these measurements demonstrate that NV centers could offer a significant improvement in thermal sensitivity relative to alternative nanoscale fluorescence thermometers (3, 4, 8–10). Even longer coherence times approaching ~1 ms, achieved through the application of higher-order decoupling sequences or the use of isotopically purified

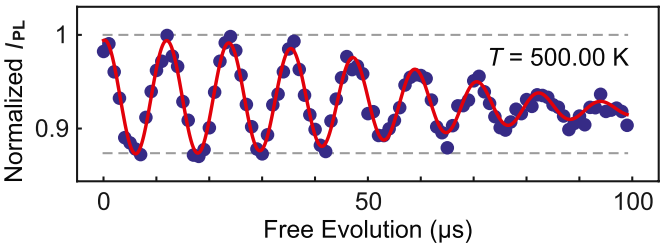

Fig. 4. A thermal echo measurement performed at 500.00 K. Here Ω_{REF}, 2.84818 GHz, has been adjusted to compensate for the large shift in D such that a detuning of ~80 kHz is achieved. The uncertainties in I_{PL}, estimated from the photon shot noise, are ~0.007. The measurement shows a reduced I_{PL} contrast between the spin states, primarily due to an increased fluorescence background on this sample at elevated temperatures. However, the larger thermal shifts in D (−140 kHz/K at 500 K) (ref. 19) largely compensate for this reduction to produce an inferred η of 39 ± 6 mK·Hz$^{-1/2}$ for this measurement. The projected η for enhanced photon collection efficiencies is ~11 mK·Hz$^{-1/2}$.

diamond to eliminate the ^{13}C spin bath (36), could further improve the thermal sensitivities from those discussed here.

Finally, to demonstrate the versatility of these NV center thermometry techniques, we perform a similar TE measurement at 500 K (Fig. 4). This measurement shows a coherence similar to that of the 300-K thermal echoes as expected from the temperature independence of the ^{13}C spin bath (19) and the sufficiently long spin-lattice relaxation time (~1 ms) at this temperature (37). The 500-K TE does show a reduced fluorescence contrast, predominantly due to an increased fluorescence background at this temperature. However, this measurement still achieves a comparable η of 39 ± 6 mK·Hz$^{-1/2}$ due to the larger shift in D (−140 kHz/K at 500 K), whereas enhanced photon collection efficiencies could provide an η of ~11 mK·Hz$^{-1/2}$. The robust temperature dependence of these spin-based thermometry methods suggests they could be applied in a variety of contexts beyond intracellular sensing such as diamond-based scanning thermal microscopy (34, 38).

Conclusions

These results illustrate the NV center's promise for nanoscale thermometry applications by demonstrating dynamical decoupling techniques that harness the NV center's long spin coherence for thermal measurement. By using this quantum degree of freedom, we achieve thermal sensitivities that approach 10 mK·Hz$^{-1/2}$, demonstrating the NV center's potential to improve on existing nanoscale fluorescence thermometry techniques by an order of magnitude. Although these results are obtained using single NV centers in high-quality synthetic diamond, the development of diamond nanostructures containing highly coherent NV centers (39, 40) suggests a pathway for fabricating nanodiamonds that achieve similar sensitivities. Such nanostructures could enable high-precision thermometry in biological and microfluidic systems with subdiffraction spatial resolution defined by the size of the nanodiamonds. Furthermore, scanning thermal measurement in fluids will benefit from recent advances in the 3D spatial control and rotational control of optically trapped nanodiamonds containing NV centers (41, 42). These compelling applications suggest the potential impact of nanoscale thermometers that combine the solid-state quantum coherence of NV centers demonstrated here with the biocompatibility, hardness, and high thermal conductivity of diamond.

Methods

Temperature Sensitivity Estimates. The measurements presented here are principally concerned with determining the coherence of the TE and TCPMG-N pulse sequences. Thus, for our measurements we detune our microwave carrier frequencies from D by an amount sufficient to induce oscillations in I_{PL} as a function of t, the free evolution time. We fit the finite-field results to functions of the form

$$I_{PL} = a\,\exp\left(-\left(\frac{t}{\tau_{1/e}}\right)^m\right)\cos(\omega t+\varphi)+b, \quad [2]$$

where $\tau_{1/e}$ is the 1/e decay time and a, m, ω, φ, and b are free parameters. We fit the near-zero-field data to functions of the form

$$I_{PL} = a\,\exp\left(-\left(\frac{t}{\tau_{1/e}}\right)^m\right)\left(\frac{1}{4}+\cos(\omega t+\varphi)\right)+b \quad [3]$$

to account for the fact that the $\pi/4$ pulse initializes the spin into $\frac{-i}{2}|1\rangle+\frac{-i}{2}|-1\rangle+\frac{1}{\sqrt{2}}|0\rangle$, such that at long times I_{PL} decays to $\frac{3}{8}I_{PL}(m_S=0)+\frac{5}{8}I_{PL}(m_S=\pm1)$. From our measurements we also extract the number of photons per measurement shot for the bright and dark spin states (p_0 and p_1, respectively). We use this information to quantify η, defined as a signal-to-noise ratio of one, using an expression analogous to those considered for NV center magnetic sensing (16, 21),

$$\eta = \sqrt{\frac{2(p_0+p_1)}{(p_0-p_1)^2}}\,\frac{1}{2\pi\,\frac{dD}{dT}\exp\left(-\left(\frac{t}{\tau_{1/e}}\right)^m\right)\sqrt{t}} \quad [4]$$

where the η values quoted in the main text correspond to the maximum value of $\exp\left(-\left(\frac{t}{\tau_{1/e}}\right)^m\right)\sqrt{t}$. In our experiments we obtain p_0 and p_1 values of ~0.007 and ~0.005, respectively; for the case of optimized photon collection efficiencies we assume values of ~0.09 and ~0.065 (26, 34). In addition to assuming that measurements are performed by monitoring I_{PL} at the optimal t, Eq. **4** also assumes the limit of small detunings between D and Ω_{REF} and that the initialization and readout microwave pulses are phase shifted by 90° so that a linear relationship between the relative phase of the spin states and the measured I_{PL} is achieved. For an extensive discussion of these considerations in the context of NV center magnetometry, see ref. 21.

Numerical Modeling. The positions of the ^{13}C nuclear spins were randomly generated at sites inside a 70 × 70 × 70 atoms^3 diamond lattice with an abundance of 1.08%. The dipolar interactions between the NV center spin and the ^{13}C spins were considered, whereas the dipolar couplings between the nuclear spins were neglected (a good approximation for our relevant experimental times of 50–100 μs). The full quantum dynamics of the NV center electronic spin (S = 1) and the 1,200 most strongly coupled ^{13}C spins (I = 1/2) were modeled. The quantitative details of the NV center spin dynamics depend on the specific positions of the ^{13}C nuclei around the NV center and can be strongly influenced by the most proximal ^{13}C (32, 43). However, the overall shapes of the TE and TCPMG-N signals, as well as the typical timescales, are relatively consistent between different nuclear configurations. A further discussion of the NV center decoherence caused by the ^{13}C spin bath is provided in *SI Appendix*.

Note. After submission of this manuscript, two complementary preprints discussing NV center thermometry were posted online (44, 45).

ACKNOWLEDGMENTS. We thank F. J. Heremans for technical assistance and B. B. Buckley, A. L. Falk, C. G. Yale, and A. L. Yeats for helpful discussion. We acknowledge financial support from the Air Force Office of Scientific Research and the Defense Advanced Research Planning Agency. Work at Ames Laboratory was supported by the Department of Energy, Basic Energy Sciences under Contract DE-AC02-07CH11358.

1. Grattan LS, Zhang ZY (1995) *Fiber Optic Fluorescence Thermometry* (Chapman & Hall, London).
2. Aizawa H, et al. (2002) Characteristics of chromium doped spinel crystals for a fiber-optic thermometer application. *Rev Sci Instrum* 73(8):3089–3092.
3. Brites CDS, et al. (2012) Thermometry at the nanoscale. *Nanoscale* 4(16):4799–4829.
4. Jaque D, Vetrone F (2012) Luminescence nanothermometry. *Nanoscale* 4(15):4301–4326.
5. Walker GW, et al. (2003) Quantum-dot optical temperature probes. *Appl Phys Lett* 83(17):3555–3557.
6. Vetrone F, et al. (2010) Temperature sensing using fluorescent nanothermometers. *ACS Nano* 4(6):3254–3258.

7. Gota C, Okabe K, Funatsu T, Harada Y, Uchiyama S (2009) Hydrophilic fluorescent nanogel thermometer for intracellular thermometry. *J Am Chem Soc* 131(8): 2766–2767.
8. Okabe K, et al. (2012) Intracellular temperature mapping with a fluorescent polymeric thermometer and fluorescence lifetime imaging microscopy. *Nat Commun* 3:705.
9. Donner JS, Thompson SA, Kreuzer MP, Baffou G, Quidant R (2012) Mapping intracellular temperature using green fluorescent protein. *Nano Lett* 12(4):2107–2111.
10. Yang JM, Yang H, Lin LW (2011) Quantum dot nano thermometers reveal heterogeneous local thermogenesis in living cells. *ACS Nano* 5(6):5067–5071.
11. van Oort E, Manson NB, Glasbeek M (1988) Optically detected spin coherence of the diamond N-V centre in its triplet ground state. *J Phys Chem* 21(23):4385–4391.
12. Gruber A, et al. (1997) Scanning confocal optical microscopy and magnetic resonance on single defect centers. *Science* 276(5321):2012–2014.
13. Jelezko F, et al. (2004) Observation of coherent oscillation of a single nuclear spin and realization of a two-qubit conditional quantum gate. *Phys Rev Lett* 93(13):130501.
14. Hong S, et al. (2013) Nanoscale magnetometry with NV centers in diamond. *MRS Bull* 38(02):155–161.
15. Grinolds MS, et al. (2013) Nanoscale magnetic imaging of a single electron spin under ambient conditions. *Nat Phys* 9(4):215–219.
16. Mamin HJ, et al. (2013) Nanoscale nuclear magnetic resonance with a nitrogen-vacancy spin sensor. *Science* 339(6119):557–560.
17. Staudacher T, et al. (2013) Nuclear magnetic resonance spectroscopy on a (5-nanometer)3 sample volume. *Science* 339(6119):561–563.
18. Dolde F, et al. (2011) Electric-field sensing using single diamond spins. *Nat Phys* 7(6): 459–463.
19. Toyli DM, et al. (2012) Measurement and control of single nitrogen-vacancy center spins above 600 K. *Phys Rev X* 2(3):031001.
20. Acosta VM, et al. (2010) Temperature dependence of the nitrogen-vacancy magnetic resonance in diamond. *Phys Rev Lett* 104(7):070801.
21. Taylor JM, et al. (2008) High-sensitivity diamond magnetometer with nanoscale resolution. *Nat Phys* 4(10):810–816.
22. de Lange G, Wang ZH, Ristè D, Dobrovitski VV, Hanson R (2010) Universal dynamical decoupling of a single solid-state spin from a spin bath. *Science* 330(6000):60–63.
23. Ryan CA, Hodges JS, Cory DG (2010) Robust decoupling techniques to extend quantum coherence in diamond. *Phys Rev Lett* 105(20):200402.
24. Naydenov B, et al. (2011) Dynamical decoupling of a single-electron spin at room temperature. *Phys Rev B* 83(8):081201.
25. McGuinness LP, et al. (2011) Quantum measurement and orientation tracking of fluorescent nanodiamonds inside living cells. *Nat Nanotechnol* 6(6):358–363.
26. Babinec TM, et al. (2010) A diamond nanowire single-photon source. *Nat Nanotechnol* 5(3):195–199.
27. Loubser JHN, van Wyk JA (1978) Electron spin resonance in the study of diamond. *Rep Prog Phys* 41(8):1201–1248.
28. Doherty MW, et al. (2013) The nitrogen-vacancy colour centre in diamond. *Phys Rep*, 10.1016/j.physrep.2013.1002.1001.
29. Fang K, et al. (2013) High-sensitivity magnetometry based on quantum beats in diamond nitrogen-vacancy centers. *Phys Rev Lett* 110:130802.
30. Slichter CP (1990) *Principles of Magnetic Resonance* (Springer, New York), 3rd Ed.
31. Haeberlen U (1976) *High Resolution NMR in Solids: Selective Averaging* (Academic, New York).
32. Childress L, et al. (2006) Coherent dynamics of coupled electron and nuclear spin qubits in diamond. *Science* 314(5797):281–285.
33. Reinhard F, et al. (2012) Tuning a spin bath through the quantum-classical transition. *Phys Rev Lett* 108(20):200402.
34. Maletinsky P, et al. (2012) A robust scanning diamond sensor for nanoscale imaging with single nitrogen-vacancy centres. *Nat Nanotechnol* 7(5):320–324.
35. Hodges JS, et al. (2013) Timekeeping with electron spin states in diamond. *Phys Rev A* 87:032118.
36. Balasubramanian G, et al. (2009) Ultralong spin coherence time in isotopically engineered diamond. *Nat Mater* 8(5):383–387.
37. Jarmola A, Acosta VM, Jensen K, Chemerisov S, Budker D (2012) Temperature- and magnetic-field-dependent longitudinal spin relaxation in nitrogen-vacancy ensembles in diamond. *Phys Rev Lett* 108(19):197601.
38. Majumdar A, et al. (1995) Thermal imaging by atomic-force microscopy using thermocouple cantilever probes. *Rev Sci Instrum* 66(6):3584–3592.
39. Hodges JS, et al. (2012) Long-lived NV- spin coherence in high-purity diamond membranes. *New J Phys* 14:093004.
40. Ohno K, et al. (2012) Engineering shallow spins in diamond with nitrogen delta-doping. *Appl Phys Lett* 101:082413.
41. Horowitz VR, Alemán BJ, Christle DJ, Cleland AN, Awschalom DD (2012) Electron spin resonance of nitrogen-vacancy centers in optically trapped nanodiamonds. *Proc Natl Acad Sci USA* 109(34):13493–13497.
42. Geiselmann M, et al. (2013) Three-dimensional optical manipulation of a single electron spin. *Nat Nanotechnol* 8(3):175–179.
43. Dobrovitski VV, Feiguin AE, Awschalom DD, Hanson R (2008) Decoherence dynamics of a single spin versus spin ensemble. *Phys Rev B* 77(24):245212.
44. Neumann P, et al. (2013) High precision nanoscale temperature sensing using single defects in diamond. arXiv:1304.0688.
45. Kucsko G, et al. (2013) Nanometer scale quantum thermometry in a living cell. arXiv: 1304.1068.